

# PhysRFANet: Physics-Guided Neural Network for Real-Time Prediction of Thermal Effect During Radiofrequency Ablation Treatment

Minwoo Shin<sup>a</sup>, Minjee Seo<sup>a</sup>, Seonaeng Cho<sup>a</sup>, Juil Park<sup>b</sup>, Joon Ho Kwon<sup>b</sup>, Deukhee Lee<sup>c,d</sup>, and Kyungho Yoon<sup>\*a</sup>

<sup>a</sup>School of Mathematics and Computing, Yonsei University, Seoul, South Korea

<sup>b</sup>Department of Radiology, Yonsei University College of Medicine, Seoul, South Korea

<sup>c</sup>Center for Healthcare Robotics, Korea Institute of Science and Technology, Seoul, South Korea

<sup>d</sup>Yonsei-KIST Convergence Research Institute, Yonsei University, Seoul, South Korea

## Abstract

Radiofrequency ablation (RFA) is a widely used minimally invasive technique for ablating solid tumors. Achieving precise personalized treatment necessitates feedback information on *in situ* thermal effects induced by the RFA procedure. While computer simulation facilitates the prediction of electrical and thermal phenomena associated with RFA, its practical implementation in clinical settings is hindered by high computational demands. In this paper, we propose a physics-guided neural network model, named PhysRFANet, to enable real-time prediction of thermal effect during RFA treatment. The networks, designed for predicting temperature distribution and the corresponding ablation lesion, were trained using biophysical computational models that integrated electrostatics, bio-heat transfer, and cell necrosis, alongside magnetic resonance (MR) images of breast cancer patients. Validation of the computational model was performed through experiments on *ex vivo* bovine liver tissue. Our model demonstrated a 96% Dice score in predicting the lesion volume and an RMSE of 0.4854 for temperature distribution when tested with foreseen tumor images. Notably, even with unforeseen images, it achieved a 93% Dice score for the ablation lesion and an RMSE of 0.6783 for temperature distribution. All networks were capable of inferring results within 10 ms. The presented technique, applied to optimize the placement of the electrode for a specific target region, holds significant promise in enhancing the safety and efficacy of RFA treatments.

## 1 Introduction

Radiofrequency ablation (RFA) stands as a pivotal technique in the field of interventional medicine due to its ability to treat various medical conditions, particularly tumors, with minimal invasiveness [1, 2, 3, 4]. RFA uses the heat generated from electrical currents delivered through percutaneously inserted electrodes to induce coagulative necrosis in pathological tissues [5]. Its significance lies in its effectiveness in eradicating a tumor while preserving healthy surrounding tissues, thus offering advantages compared to the traditional surgical resection, such as quick recovery, high efficacy, low complication rate, and cost-effectiveness [6, 7, 8].

To achieve precise treatment, interventional radiologists adjust clinical settings such as applied power, current duration, and the insertion trajectory of electrodes [9, 10, 11]. However, quantitatively predicting the extent of ablation remains a challenging task, as treatment outcomes are influenced not only by device settings but also by individual-specific characteristics and the surgeon's expertise. In general planning procedures, ablation shapes are commonly assumed to be ellipsoids, based on manufacturer-provided

---

\*[yoonkh@yonsei.ac.kr](mailto:yoonkh@yonsei.ac.kr)

ablation size guidelines designed primarily for homogeneous tissue. This approach overlooks patient-specific factors crucial for achieving personalized and precise RFA treatment [12, 13].

Theoretical models and computer simulations serve as crucial tools in predicting the ablated region and improving therapeutic outcomes for individual patients by providing vital information into the electrical and thermal behaviors during RFA procedure [8, 14, 15, 16, 17]. The outcomes of temperature distribution and the corresponding ablation lesion are obtained through analysis of multi-biophysics models, which represent electrical conduction, bio-heat transfer, and cell necrosis process [18, 19, 20]. However, achieving accurate predictions demands a significant computational cost, thereby imposing constraints on its practical application in clinical settings [21].

Several efforts have been made to enhance simulation speed for the intra-operative utilization of computational methods during RFA procedures [22, 23, 24]. These works have achieved significant reductions in computation time owing to the use of massively parallel computing on graphics processing units (GPU). However, even with these advancements, the simulation times still range from a few seconds to minutes, depending on the size of the simulation domain. Furthermore, prolonged simulation times become necessary when utilizing more sophisticated models, such as coupled multi-physics analysis [25] and considering the phase change effect of biological tissue [26].

Recently, there has been an emerging trend to leverage deep learning algorithms for the efficient representation of complex physical phenomena that pose challenges for characterization through traditional mathematical analysis [27, 28, 29, 30, 31]. Within the domain of RFA treatment, a noteworthy study by [32] exemplifies the potential of implementing real-time estimation of RFA lesion depth using a machine learning model combined with a statistical merging approach. The proposed system utilized multi-frequency impedance measurement data, achieving accuracy at the millimeter resolution. However, it is limited by providing only one-dimensional depth information of RFA lesions in a simplistic tissue representation model. For the practical efficacy of such deep learning models in clinical settings, it is essential to accurately represent the multi-physics phenomena arising from the intricate morphologies of lesions.

In this paper, we present PhysRFANet, a set of deep neural networks designed to learn from computational simulations that capture the multi-physics phenomena inherent in RFA procedures. The training data were generated through computational simulations of electrostatic, bio-heat transfer, and cell necrosis models using magnetic resonance (MR) images obtained from 11 actual breast cancer patients. The accuracy of the computational model was validated through experiments using *ex vivo* bovine liver tissue. We developed a total of six network models based on three different architectures, each serving two specific purposes: predicting temperature distribution and the corresponding ablation lesion. The performance of these network models was evaluated using various metrics. Additionally, to evaluate the robustness and generality of our model, we conducted further assessments using two new sets of patient data that were entirely excluded from the training process. The significance of the proposed model is summarized as follows:

- The computational biophysical model reflects the geometric characteristics of an individual patient’s tumor through a magnetic resonance (MR) image.
- Prediction accuracy of the computational model was validated using *ex vivo* bovine liver tissue.
- Neural network models were trained on the results of the computational model.
- Real-time personalized predictions of thermal distribution and cell necrosis regions are available, given the tumor geometry and electrode placement.

## 2 Computational model

In this section, we address the formulation of our computational model, which includes a geometric representation of tumor tissue, an electrical field calculation, a bio-heat transfer algorithm, and a cell necrosis model.

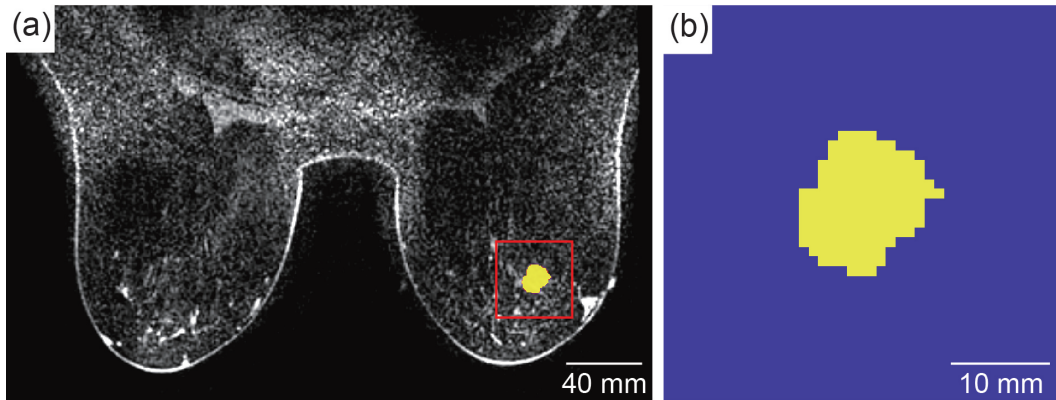


Figure 1: An example of tumor geometric modeling from an MR image. (a) Overlay of tumor segmentation result (yellow region) onto the corresponding axial view MR image. The red box shows the boundary of the cropped field-of-view, and (b) shows the segmentation image in the field-of-view. The yellow region represents the tumor area, while the blue region is normal tissue.

## 2.1 Tumor geometric model via MR image

MR images of thirteen breast cancer patients from a publicly available dataset [33] were utilized to model tumor geometry. The datasets consisted of dynamic contrast enhanced (DCE) MR images and the corresponding segmentation images which were annotated by radiologists to depict the cancerous regions for each patient. All images were resampled to isotropic voxels of  $1.0 \times 1.0 \times 1.0 \text{ mm}^3$  using the Lanczos filter algorithm [34]. For computational efficiency, the simulation domain for each patient was defined by cropping it to the field-of-view centered at the volumetric center of the tumor region with a size of  $40 \times 40 \times 40 \text{ mm}^3$ . The field-of-view size was sufficient to encompass the entire volume of the segmented tumor ( $3,021 \pm 2,789 \text{ mm}^3$ ,  $N=13$ ). A visual representation of the tumor geometric model using MR images is provided in Fig. 1.

## 2.2 Electro-static analysis for electrical field

The quasi-static version of Maxwell's equation is used to compute the resistive heating during RFA. This is relevant because, within the RFA frequency range of 450 to 550 kHz, the electric field's wavelength is substantially larger than the size of the active electrode, as noted in [35]. Thus, the electric potential is determined by solving the generalized Laplace equation

$$\nabla \cdot (\sigma \nabla V) = 0 \text{ in } \Omega, \quad (1)$$

where  $\sigma$  is the electrical conductivity (S/m),  $V$  is the electric potential (V) with the following boundary conditions, and  $\Omega$  is a volumetric domain for analysis [36]:

$$\begin{cases} V(\mathbf{x}) = V_p, & \mathbf{x} \in \Gamma_e, \\ \mathbf{n}(\mathbf{x}) \cdot \nabla V(\mathbf{x}) = 0, & \mathbf{x} \in \Gamma_s \end{cases} \quad (2a)$$

where  $V_p$  is the applied power (W),  $\Gamma_e$  is the boundary of the domain covered by the electrodes, and  $\Gamma_s$  is the exterior surface boundary of simulation space.

The finite element formulation of Eq. (1) and (2) is as follows:

$$\int_{\Omega} \sigma \delta \mathbf{V}^T \left( \frac{\partial \mathbf{N}^T}{\partial x} \frac{\partial \mathbf{N}}{\partial x} + \frac{\partial \mathbf{N}^T}{\partial y} \frac{\partial \mathbf{N}}{\partial y} + \frac{\partial \mathbf{N}^T}{\partial z} \frac{\partial \mathbf{N}}{\partial z} \right) \mathbf{V} d\Omega = 0, \quad (3)$$

where  $\mathbf{V}$  is the discretized electrical potential at finite element nodes,  $\mathbf{N}$  is a linear interpolation matrix (i.e.,  $V = \mathbf{N}\mathbf{V}$ ), and  $\delta$  indicates a variational symbol. Through the standard finite element solution procedure with Eq. (3), the solution of electrical potential is obtained.

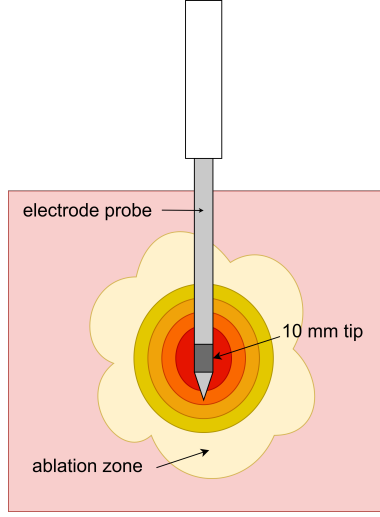


Figure 2: The illustration represents a single-needle ablation electrode utilized for tumor ablation. A source voltage applied to the conductive tip facilitates the therapeutic intervention.

The volumetric heat source due to resistive heating during RFA, denoted by  $Q_r$  ( $\text{W}/\text{m}^3$ ), is quantified by

$$Q_r = \sigma |\nabla V|^2. \quad (4)$$

The calculated  $Q_r$  is utilized as the heat input for the bio-heat transfer analysis.

Finite element models were constructed based on the obtained tumor geometry in Section 2.1. The meshes corresponding to the tumor tissue were assigned an electrical conductivity of 4 S/m, while the finite elements classified as normal tissue had an electrical conductivity of 0.4 S/m [37]. The input voltage generated by an electrode tip with a length of 10 mm and a diameter of 1 mm was modeled by applying boundary conditions in Eq. (2a) to all nodes encompassed by the electrode. Located at the end of the needle, the electrode tip releases high-frequency alternating current into the surrounding tissue, generating heat through radiofrequency energy. An illustration of a single-needle ablation electrode is presented in Fig. 2.

### 2.3 Bio-heat transfer analysis for heat propagation

Pennes bioheat model is used to model the bio-heat transfer inside the breast tissue during RFA [38]:

$$\rho c \frac{\partial T}{\partial t} = \nabla \cdot (k \nabla T) + \rho_b c_b \omega_b (T_b - T) + Q_m + Q_r, \quad (5)$$

where  $\rho$  is the density of tissue ( $\text{kg}/\text{m}^3$ ),  $c$  is the specific heat capacity of tissue ( $\text{J}/\text{kg}/\text{K}$ ),  $T$  is temperature ( $^\circ\text{C}$ ),  $t$  is ablation time,  $k$  is thermal conductivity of tissue ( $\text{W}/\text{m}/\text{K}$ ),  $\rho_b$  is the density of blood,  $c_b$  is the specific heat of blood,  $\omega_b$  is the perfusion rate of blood,  $T_b$  is the temperature of blood ( $37^\circ\text{C}$ ),  $Q_m$  is metabolic heat generation ( $\text{W}/\text{m}^3$ ), and  $Q_r$  is resistive heat generation obtained from Eq. (4) ( $\text{W}/\text{m}^3$ ).

To numerically solve Eq. (5), the finite difference time domain (FDTD) scheme is used [8, 39, 40],

$$\begin{aligned} & \frac{\rho_{i,j,k} c_{i,j,k}}{\Delta t} (T_{i,j,k}^{t+\Delta t} - T_{i,j,k}^t) \\ &= \frac{k_{i,j,k}}{\Delta s^2} [(T_{i+1,j,k}^t - T_{i,j,k}^t) - (T_{i,j,k}^t - T_{i-1,j,k}^t)] \\ &+ \frac{k_{i,j,k}}{\Delta s^2} [(T_{i,j+1,k}^t - T_{i,j,k}^t) - (T_{i,j,k}^t - T_{i,j-1,k}^t)] \\ &+ \frac{k_{i,j,k}}{\Delta s^2} [(T_{i,j,k+1}^t - T_{i,j,k}^t) - (T_{i,j,k}^t - T_{i,j,k-1}^t)] \\ &+ \rho_b c_b \omega_b (T_b - T_{i,j,k}^t) + Q_{m;i,j,k} + Q_{r;i,j,k}, \end{aligned} \quad (6)$$

where  $\Delta t$  is the discretized time interval,  $\rho_{i,j,k}$ ,  $c_{i,j,k}$ ,  $T_{i,j,k}$ ,  $k_{i,j,k}$ ,  $Q_{m;i,j,k}$ , and  $Q_{r;i,j,k}$  are respectively the density, specific heat capacity, temperature, thermal conductivity, metabolic heat generation, and

resistive heat generation of tissue at the grid index  $i, j, k$  of the simulation domain, and  $\Delta s$  is the spatial discretization interval (i.e., grid interval).

Based on the segmented MR image in Section 2.1, thermal properties of the tumor tissue (density of  $1,050 \text{ kg/m}^3$ , specific heat capacity of  $3,770 \text{ J/kg/K}$ , thermal conductivity of  $0.48 \text{ W/m/K}$ ), normal tissue (density of  $911 \text{ kg/m}^3$ , specific heat capacity of  $2,348 \text{ J/kg/K}$ , thermal conductivity of  $0.21 \text{ W/m/K}$ ), blood perfusion (blood density of  $1,050 \text{ kg/m}^3$ , blood specific heat capacity of  $3,617 \text{ J/kg/K}$ , blood perfusion rate of  $5.3 \text{ s}^{-1}$  for tumor tissue, blood perfusion rate of  $0.2 \text{ s}^{-1}$  for normal tissue), and metabolic heat ( $400 \text{ W/m}^3$  for normal tissue and  $13,600 \text{ W/m}^3$  for tumor tissue) were assigned to the simulation [20]. The initial temperature of the tissue and blood was set to  $37^\circ\text{C}$ . The simulations were conducted by applying the resistive heat (i.e.,  $Q_{m;i,j,k}$ ) for 180 seconds with a time resolution (i.e.,  $\Delta t$ ) of 0.1 seconds and calculating the temperature distribution of the entire spatial domain at each time interval.

## 2.4 Cell necrosis model

The thermal damage of biological tissue ( $\Psi$ ) is quantified using the first-order Arrhenius rate equation as follows [20]:

$$\Psi(t) = \int_0^t A \exp\left(\frac{-E_a}{RT(t)}\right) dt, \quad (7)$$

where  $A$  is the frequency factor ( $= 1.18 \times 10^{44}$ ),  $E_a$  is the activation energy for irreversible damage reaction ( $= 3.02 \times 10^5 \text{ J/mol}$ ),  $R$  is the universal gas constant ( $= 8.3134 \text{ J/mol/K}$ ),  $T$  is the temperature (K) of the corresponding tissue.

The temperature distribution for each time step obtained in Section 2.3 was utilized to evaluate the cumulative tissue damage values of  $\Psi(t)$  for every voxel. To delineate irreversible thermal damage, we applied a threshold of  $\Psi(t) > 1$ , classifying values exceeding this threshold as the damaged tissue region and values below it as the viable tissue region [41].

## 2.5 Experimental validation

In this section, we describe the experiment setup for RFA, designed to validate the accuracy and reliability of our RFA computational model. Freshly excised bovine liver, procured on the day of the experiment from a local butcher shop, served as the experimental tissue. Ten cuboid-shaped samples, each measuring approximately  $10 \times 10 \times 10 \text{ cm}^3$ , were prepared by cutting the bovine liver to fit within a custom-designed 3D-printed container shown in Fig. 3(a). This container is designed to facilitate precise RF ablation at the center of the liver sample, followed by a subsequent halving of the sample at the same location, as illustrated in Fig. 3(b).

A 17-gauge monopolar electrode with a tip length of 10 mm (V-tip, RF medical, Seoul, Korea) was inserted to a depth of approximately 5 cm, positioned at the center of the liver sample. Radiofrequency waves were emitted from the electrode tip into the surrounding tissue for 3 minutes, utilizing a 200 W generator (M-3004, RF medical, Seoul, Korea). After completing the ablation, the electrode was removed, and the bovine liver sample was bisected to obtain cross-sectional plane images. Distinct areas of coagulative necrosis were revealed in these images, identified and segmented using the ‘‘Segment Anything in Medical Images’’ code [42, 43] for subsequent quantitative analysis.

Through the obtained experimental results, the proposed computational model was validated. A homogeneous tissue space with a resolution of 1 mm, spanning  $40 \times 40 \times 40 \text{ mm}^3$ , was utilized, with an electrode placed at the central location of the simulation space. The electrical conductivity of the bovine liver tissue was set to  $0.69 \text{ S/m}$  [44]. The thermal properties of the tissue included a density of  $1079 \text{ kg/m}^3$ , a specific heat capacity of  $3415.0 \text{ J/kg/K}$ , and a thermal conductivity of  $0.5 \text{ W/m/K}$  [45]; blood perfusion and metabolic heat terms were disregarded. The heat generated by radiofrequency energy was applied over a total duration of 180 seconds, using a time step of 0.1 seconds, starting from an initial temperature of  $20^\circ\text{C}$ .

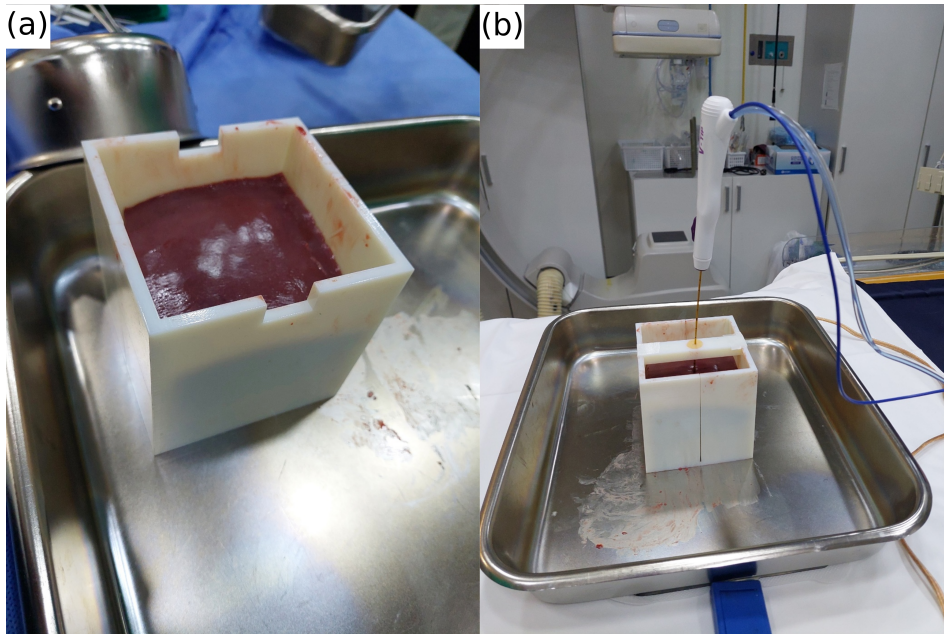


Figure 3: Experimental setup for *ex vivo* tissue RFA. (a) A bovine liver sample is cut into a cuboidal shape and carefully placed within a 3D-printed container, (b) enabling accurate ablation at its center.

### 3 Neural network models

In this section, we employed three network models with different architecture for performance comparisons. Specifically, for the purpose of basic performance benchmarking, the encoder-decoder based CNN (EDCNN) architecture was employed. The U-Net architecture, with its symmetric encoder-decoder structure complemented by skip connections, is our primary focus in this research. This design is known for its use of skip connections that combine deep coarse-grained feature maps from the decoder and the shallow fine-grained feature maps from the encoder, effectively enhancing target details [46, 47, 48, 49, 50, 51].

#### 3.1 Training and test data generation

The datasets used to train and test the network model are derived from the computational model described in Section 2. To ensure a diverse dataset, we conducted RFA simulations for each breast tumor MR image, utilizing 500 randomly placed electrode tip locations and directions within the tumor regions. The segmented breast tumor images (size of  $41 \times 41 \times 41$ ) along with binary images (size of  $41 \times 41 \times 41$ ) representing the placement of electrode tip were utilized as the network inputs, and either the corresponding coagulative tissue necrosis zones (size of  $41 \times 41 \times 41$ ) or temperature distributions (size of  $41 \times 41 \times 41$ ) obtained from RFA simulation were respectively employed for the network output.

For the training datasets, we collected 5,500 RFA simulation results derived from eleven distinct breast tumor images (BT1-BT11) from different patients. This data was then randomly split into 5,000 samples for training and 500 for testing purposes. Out of the 5,000 training data samples, 200 were allocated to the validation set for fine-tuning. On the other hand, to evaluate the network’s performance on unseen MR images of breast tumors from a practical perspective, we utilized 500 RFA simulation results sourced from two distinct tumors (BT12 and BT13), each from a separate patient, as another test dataset. For a better understanding, please refer to Table 1.

In the training of our PhysRFANet, we carefully selected various hyperparameters to optimize performance. In configuring our model’s optimization strategy, we selected the Adam optimizer, initialized with a learning rate of 0.001, and set the batch size to 16 for efficient processing. To fine-tune the learning rate during training, we implemented the “ReduceOnPlateau” learning rate scheduler. This scheduler was configured to reduce the learning rate by a factor of 0.5 if no improvement is observed in

the valid loss over 5 epochs. This approach allows for dynamic adjustment of the learning rate based on the model’s performance. The training was conducted over 100 epochs. All training was performed on a single GPU, utilizing its parallel processing capabilities to expedite the training process.

### 3.2 Network architectures for the coagulative necrosis

In this section, we provide a thorough overview of the PhysRFANet architectures, showcasing them with visual diagrams complemented by in-depth explanations. Visual explanation is provided in Fig. 4. Each component and layer will be detailed, emphasizing their specific roles and contributions to the overall system, as evidenced by ablation studies.

The EDCNN model, shown in Fig. 4(a), is a CNN specifically tailored for 3D data. It consists of an encoder and a decoder: the encoder is a series of 3D convolutional layers, each followed by batch normalization and ReLU activation, designed to extract and compress features from the input. The encoder uses strides to reduce spatial dimensions, akin to downsampling. The decoder part, aimed at reconstructing the data to a higher resolution, employs transposed 3D convolutional layers, also accompanied by batch normalization and ReLU activations. In its forward pass, the model concatenates two types of input data, indicating its capability to handle dual input modalities, a common scenario in medical imaging tasks. The final layers reduce the channel dimension to one to match the size of the input. Additionally, the model adopts specific weight initialization strategies for its layers, indicating a focus on efficient training convergence.

The U-Net architecture, shown in Fig. 4(b), includes the decoder, mid-layers, and encoder classes. The decoder performs downsampling, mid-layers process features at the network bottleneck, and the encoder handles the upsampling part. These modules use convolutional layers, batch normalization, and activation functions suitable for processing 3D data. The U-Net architecture concatenates and processes inputs through the downscaling, middle, and upscaling modules. The architecture is designed for tasks that involve volumetric data.

The Attention U-Net model, shown in Fig. 4(c), is a sophisticated neural network architecture that blends the U-Net structure with self-attention mechanisms. This design is especially suitable for complex applications like medical image analysis, which require both local and global contextual understanding. The network features self-attention modules that implement multi-head attention for capturing long-range dependencies within the data, accompanied by layer normalization and feedforward networks for further refinement. The architecture is structured along a U-Net framework, with the encoder constituting the downsampling path. These modules employ 3D convolutions, batch normalization, and LeakyReLU activations to incrementally extract complex features while reducing spatial dimensions. In the middle of the network, mid-layers process these features, employing skip connections for added efficiency. The upsampling path, composed of a decoder, increases the spatial dimensions and integrates features from the downsampling path, enhancing detail retention. Crucially, self-attention modules are interspersed in the upsampling path, augmenting the network’s focus on salient features. The forward method defines the workflow, starting with the concatenation of two input data types and proceeding through the successive network layers, with optional interpolation of input and output to specific dimensions.

### 3.3 Network architectures for the temperature distribution

The same network architectures described in Section 3.2 are utilized for analyzing the temperature distribution. The primary distinction between the networks shown in Fig. 4(a) and Fig. 5 lies in their

Table 1: Splitting of foreseen and unforeseen test datasets.

	training dataset	test dataset
foreseen	5000 (BT1-BT11)	500 (BT1-BT11)
unforeseen		500 (BT12-BT13)

outputs. Otherwise, the networks are largely similar, with the main differences being in their respective outputs. As in the previous section, ablation studies will be conducted to determine how the network’s performance is impacted by the change of various components.

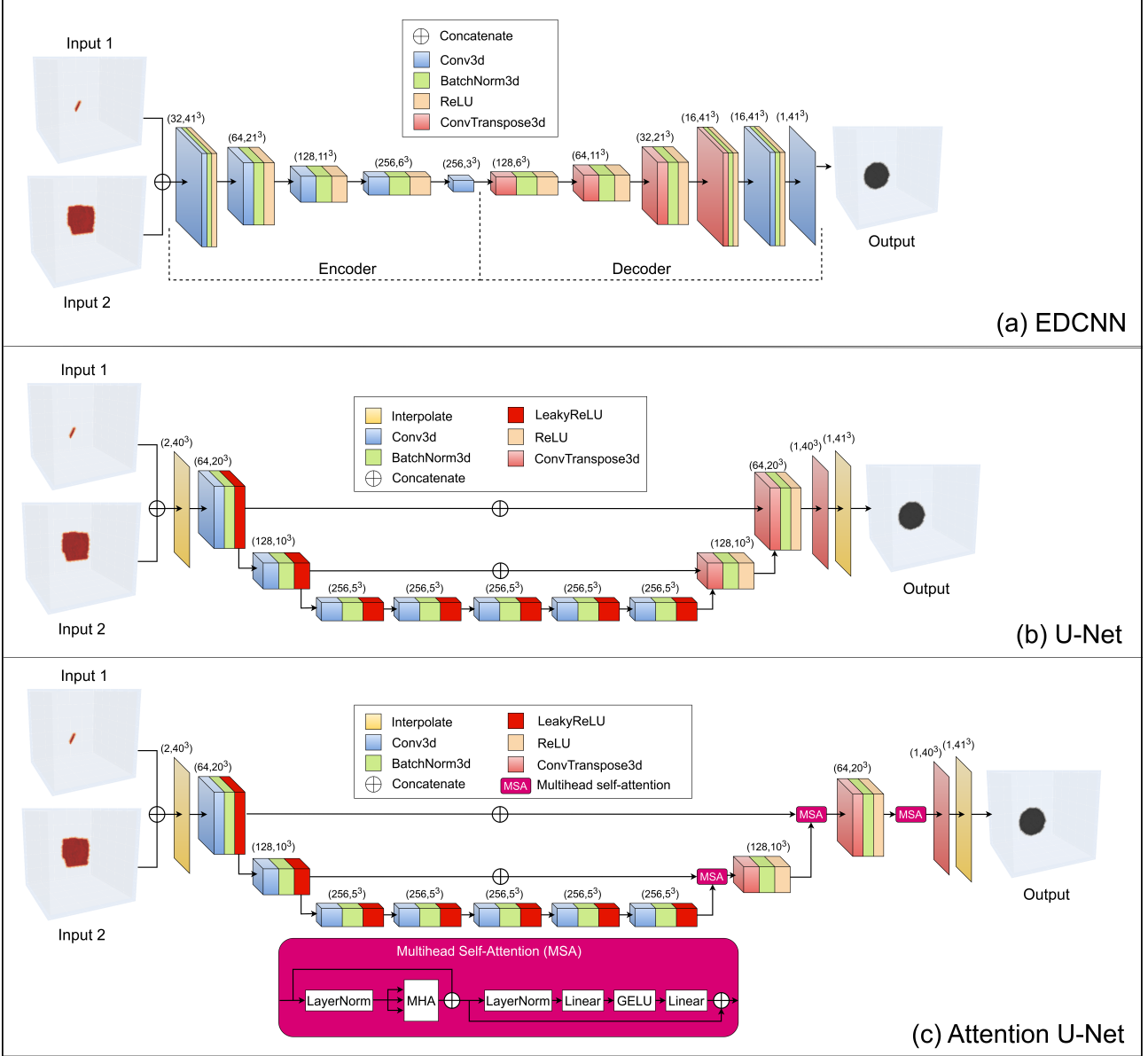


Figure 4: Three network architectures: (a) EDCNN, (b) U-Net, and (c) multihead-Attention U-Net architectures. The input 1 is the geometry of the electrode tip and the input 2 is the segmented breast tumor from the MR image. The output is the predicted ablation lesion zone. The Dice loss function is used for all network training.

### 3.4 Loss function

For the network training of the ablated lesion zone, we employ the Dice loss function, which is defined as follows:

$$\text{Dice}(x, \tilde{x}) = 1 - \frac{2 \sum_{i=1}^n x_i \tilde{x}_i}{\sum_{i=1}^n x_i^2 + \sum_{i=1}^n \tilde{x}_i^2}, \quad (8)$$

where  $\tilde{x}_i$  and  $x_i$  represent the components at the  $i$ -th position in the ground truth and the corresponding ablation lesion prediction, respectively.

For the network training of the temperature distribution, we utilize a loss function that combines mean squared error (MSE), weighted MSE, and the  $\text{Dice}_{(>50)}$  loss. To introduce a weighted MSE loss



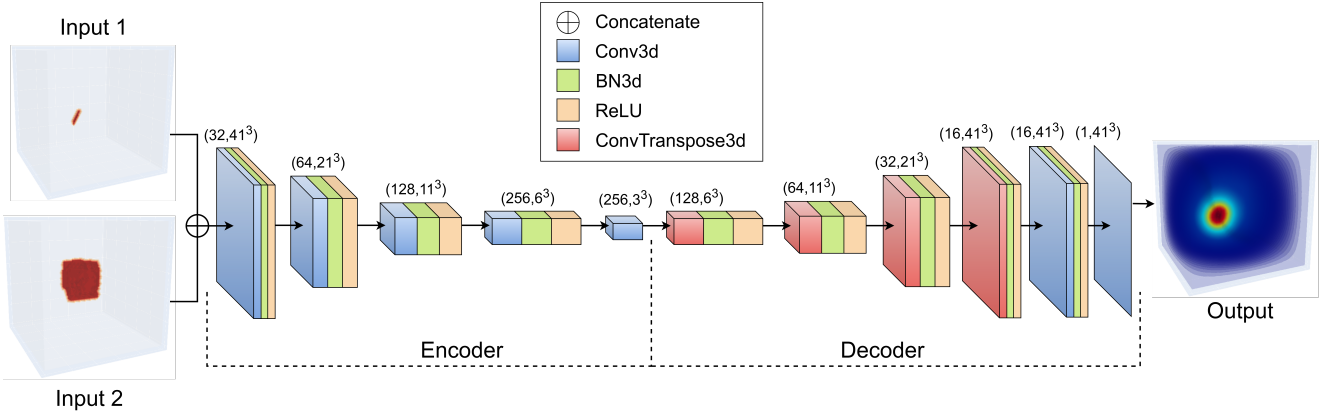


Figure 5: EDCNN architecture, where Input 1 comprises the electrode tip geometry and Input 2 is the segmented breast tumor from the MR image. The output is the predicted temperature distribution map. The U-Net and Attention U-Net architectures employed for temperature distribution prediction are identical to those in Fig. 4(b) and (c), with the primary difference being the output, which is now the temperature distribution. The combined loss function Eq. (12) with  $(\alpha, \beta, \gamma) = (0.8, 0.1, 0.1)$  is used for all network training for the temperature distribution.

function, define a mask  $m$  as follows:

$$m_i = \begin{cases} 1, & \text{if } x_i > 50^\circ\text{C}, \\ 0, & \text{otherwise.} \end{cases} \quad (9)$$

where  $\tilde{x}_i$  and  $x_i$  denote the elements at the  $i$ -th position in the ground truth and the corresponding temperature distribution prediction, respectively. We implemented the weighted MSE loss function that applies the weight  $\omega$  to the MSE loss for elements where the mask is 1 (above the threshold). The MSE loss remains unchanged where the mask is 0, enabling accurate prediction of the temperature distribution in the region of interest with elevated temperatures exceeding  $50^\circ\text{C}$ . The weighted MSE loss function is defined as

$$\mathcal{L}_1(x, \tilde{x}) = \frac{1}{n} \sum_{i=1}^n (x_i - \tilde{x}_i)^2 (\omega m_i + (1 - m_i)). \quad (10)$$

The  $\text{Dice}_{(>50)}$  loss function is defined as

$$\text{Dice}_{(>50)}(x, \tilde{x}) = 1 - \frac{2 \sum_{i=1}^n x_i (>50) \tilde{x}_i (>50)}{\sum_{i=1}^n x_i^2 (>50) + \sum_{i=1}^n \tilde{x}_i^2 (>50)}. \quad (11)$$

In particular, the  $\text{Dice}_{(>50)}$  loss function relies on the temperature ( $50^\circ\text{C}$ ) at which the cell death pattern transitions to a predominance of necrosis, as discussed in [52]. The combined loss function is as shown below:

$$\mathcal{L}(x, \tilde{x}) = \frac{\alpha}{n} \sum_{i=1}^n (x_i - \tilde{x}_i)^2 + \beta \mathcal{L}_1(x, \tilde{x}) + \gamma \text{Dice}_{(>50)}(x, \tilde{x}), \quad (12)$$

where  $x$  and  $\tilde{x}$  are predictions and ground truth, respectively, and  $\alpha$ ,  $\beta$ , and  $\gamma$  are weights.

## 4 Results

In this section, we present the evaluation metrics employed, experimental validation, and evaluate the prediction accuracy and inference time of the proposed network models. To demonstrate the robustness of the developed network, validation was also conducted using unforeseen tumor image data obtained from a new patient.

## 4.1 Evaluation metrics

Root mean squared error (RMSE), mean absolute error (MAE), and Dice score are used to evaluate test outcomes for temperature distribution. Specifically, the Dice scores, represented as  $\text{Dice}_{(>40)}$  and  $\text{Dice}_{(>50)}$ , correspond to the temperature maps exceeding  $40^\circ\text{C}$  and  $50^\circ\text{C}$ , respectively. In addition, Dice score [53, 54], Jaccard score [55], and Hausdorff distance [56] are used to evaluate test outcomes for ablation lesion. The Hausdorff distance  $d_H(X, Y)$  between two sets  $X$  and  $Y$  is defined as follows:

$$d_H(X, Y) = \max \left\{ \max_{x \in X} d(x, Y), \max_{y \in Y} d(X, y) \right\}, \quad (13)$$

where

$$d(a, B) = \min_{b \in B} d(a, b). \quad (14)$$

## 4.2 Experimental validation

In this section, we compare the outcomes of the RFA simulations with the RFA experimental results to validate the accuracy of our numerical RFA simulation. Fig. 6 presents a comparative analysis of two exemplary samples, selected from a total of seven, demonstrating simulated coagulative necrosis alongside the results of RFA experiments. Table 2 provides length measurements, both horizontally and vertically, passing through the center of gravity of the necrosis region, along with its corresponding area. The center of gravity is determined using the `scipy.ndimage.center_of_mass` function [57], and the horizontal and vertical lengths are obtained using ImageJ [58]. The results demonstrate an average accuracy within 2% on the aspect of the area.

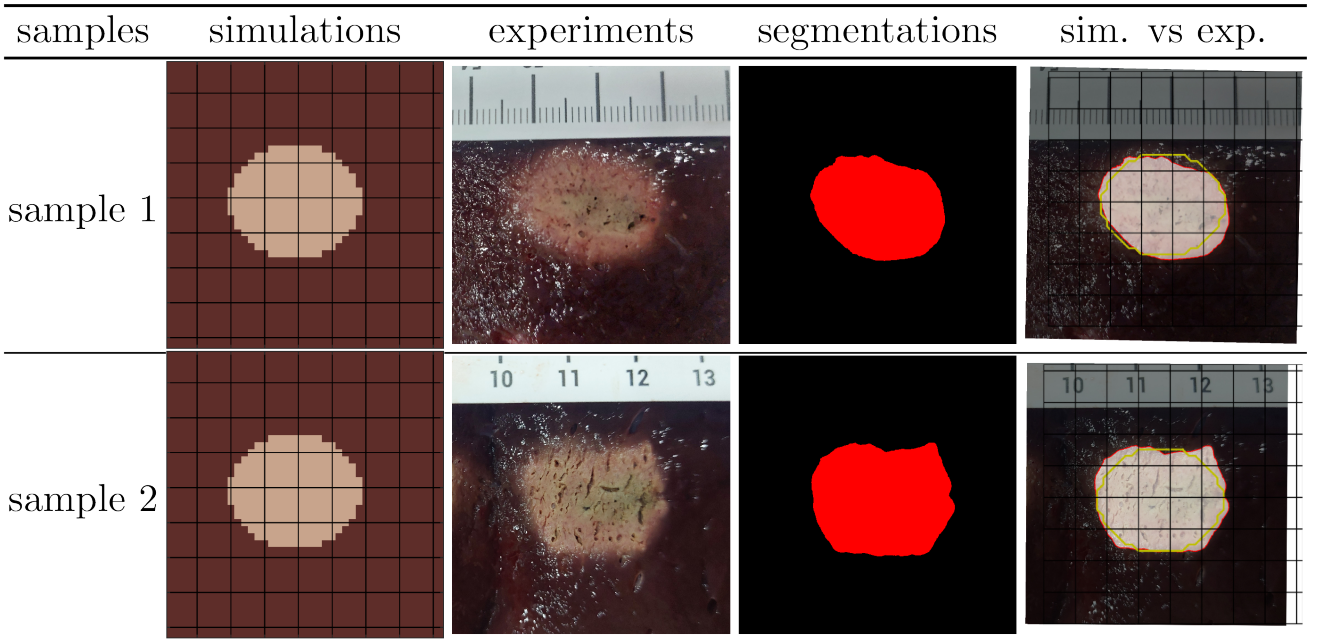


Figure 6: Comparison of simulated coagulative necrosis and RFA experiment results for two samples. The leftmost figures illustrate the numerical simulation outcomes. The second column represents experimental results. The third column shows segmented necrotic regions (red) obtained using SAM [42]. Meanwhile, the last column displays the segmented coagulative necrotic regions (red) with overlaid simulated results (yellow).

## 4.3 Evaluation of ablation lesion with foreseen/unforeseen test dataset

We present an evaluation of the RFA lesion zone, demonstrating the performance of three different network architectures using both foreseen and unforeseen test datasets. Table 3 shows the prediction

Table 2: Comparison of RFA Simulation outcomes and experimental segmentation data using diverse metrics. The term “samples” denotes the experimental sample numbers. “horizontal” and “vertical” refer to the lengths of lines, in mm. The “area”, signifies the segmentation size in  $\text{mm}^2$ .

samples	horizontal	vertical	area
1	19.67	15.87	255.71
2	20.51	15.72	304.93
3	23.12	14.03	253.33
4	17.72	12.73	212.15
5	16.12	15.73	223.52
6	21.84	16.41	307.29
7	19.51	16.69	237.29
avg $\pm$ sd	19.78 $\pm$ 2.37	15.31 $\pm$ 1.42	256.32 $\pm$ 34.56
simulation	20.00	16.00	261
difference	1.10%	4.31%	1.79%

accuracy of damaged volume for each network model under the conditions of foreseen and unforeseen datasets. In the case of testing using a foreseen dataset, both U-Net and Attention U-Net architectures demonstrated higher predictive accuracy compared to EDCNN. Specifically, U-Net and Attention U-Net exhibited nearly identical accuracy with a Dice score of 96%. On the other hand, the test using an unforeseen dataset showed slightly lower accuracy compared to the foreseen dataset tests. However, when utilizing the Attention U-Net architecture, it achieved the highest Dice accuracy of 93.6% among the tested network models for the unforeseen dataset.

Table 3: Comparison of prediction accuracy for ablation lesion zone on foreseen/unforeseen test datasets. (num\_epochs = 100)

test sets	networks	Dice	Jaccard	Hausdorff
foreseen	EDCNN	0.9388	0.8871	1.1145
	U-Net	0.9624	0.9282	1.0202
	Att. U-Net	0.9632	0.9298	1.0271
unforeseen	EDCNN	0.9061	0.8338	1.3161
	U-Net	0.9185	0.8531	3.7220
	Att. U-Net	0.9364	0.8825	1.2255

Fig. 7 shows an exemplar graphical comparison of ablation lesion predictions with an unforeseen test dataset. The upward trend in accuracy is observed across EDCNN, U-Net, and Attention U-Net, with each subsequent model exhibiting improved performance over its predecessor. Among the three models, Attention U-Net exhibits the highest accuracy, indicating a progressive enhancement in the ability to analyze and interpret data correctly with each advanced model iteration.

#### 4.4 Evaluation of temperature distribution with foreseen/unforeseen test dataset

Prior to assessing the performance of the presented network models in predicting temperature distribution, we conducted tests involving different weight distributions  $(\alpha, \beta, \gamma)$  for the combined loss function defined in Eq. (12). Table 4 indicates that  $(\alpha, \beta, \gamma) = (0.7, 0.1, 0.2)$  yields the one of the best metrics. The selection of weights  $(0.7, 0.1, 0.2)$  is appropriate as minimizing the RMSE requires alpha to be the primary factor, dominating  $\beta$  and  $\gamma$ . The small values of beta and gamma allow for slight refinements, particularly enhancing the accuracy in critical high-temperature regions. Therefore, we adopted the determined weight distribution for the weighted loss function during the training process.

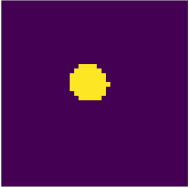

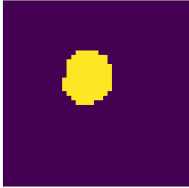
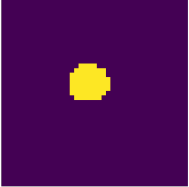
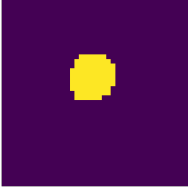
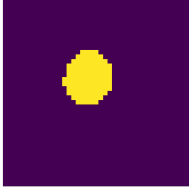
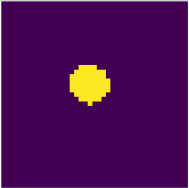
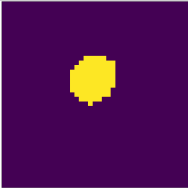
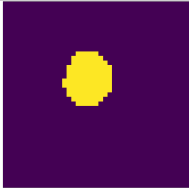
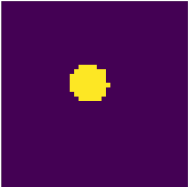

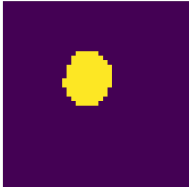
methods	xy	yz	zx	Dice	Jaccard	Hausdorff
Target						
EDCNN				0.9650	0.9323	1.0000
U-Net				0.9655	0.9332	1.0000
Att. U-Net				0.9663	0.9348	1.0000

Figure 7: Comparison of ablation lesion predictions from various networks on an unforeseen test dataset with simulation results for a single sample. A positive trend in accuracy is observed in the order of EDCNN, U-Net, and Attention U-Net.

Table 4: Comparing the performance of loss functions using different weight combinations on the foreseen test dataset. The U-Net is employed for this evaluation. (num\_epochs=30)

$(\alpha, \beta, \gamma)$	RMSE	MAE	Dice $_{(>40)}$	Dice $_{(>50)}$
(1.0, 0.0, 0.0)	0.8201	0.5059	0.9766	0.9635
(0.9, 0.1, 0.0)	0.9149	0.5827	0.9727	0.9561
(0.9, 0.0, 0.1)	0.8938	0.5551	0.9755	0.9576
(0.8, 0.2, 0.0)	0.8796	0.5419	0.9761	0.9607
(0.8, 0.1, 0.1)	0.8278	0.4956	0.9779	0.9633
(0.8, 0.0, 0.2)	1.0140	0.6689	0.9663	0.9469
(0.7, 0.3, 0.0)	1.0001	0.5962	0.9754	0.9538
(0.7, 0.2, 0.1)	0.8712	0.5463	0.9755	0.9579
(0.7, 0.1, 0.2)	0.8153	0.5026	0.9766	0.9637
(0.7, 0.0, 0.3)	0.9808	0.6550	0.9690	0.9462
(0.6, 0.4, 0.0)	0.9285	0.5730	0.9739	0.9582
(0.6, 0.3, 0.1)	0.9480	0.5852	0.9746	0.9525
(0.6, 0.2, 0.2)	0.9036	0.5652	0.9733	0.9572
(0.6, 0.1, 0.3)	1.0684	0.6888	0.9673	0.9488
(0.6, 0.0, 0.4)	0.8569	0.5328	0.9755	0.9602

Table 5 shows the prediction accuracy of temperature distribution for each network model under the conditions of foreseen and unforeseen datasets. In the case of a test using the foreseen datasets, it is observed that Attention U-Net achieves the highest accuracy among the three network architectures, with an RMSE of 0.4854. In the case of unforeseen results, there was a slight decrease in prediction accuracy compared to the foreseen test results. However, when utilizing the Attention U-Net architecture, a still notable accuracy of 0.6783 in RMSE was observed.

Table 5: Performance comparisons of temperature distribution on a foreseen/unforeseen test dataset.

test sets	networks	RMSE	MAE	Dice <sub>(&gt;40)</sub>	Dice <sub>(&gt;50)</sub>
foreseen	EDCNN	0.6653	0.4203	0.9779	0.9625
	U-Net	0.4853	0.2576	0.9887	0.9844
	Att. U-Net	0.4854	0.2560	0.9892	0.9839
unforeseen	EDCNN	1.0502	0.7135	0.9564	0.9203
	U-Net	0.7340	0.4587	0.9793	0.9578
	Att. U-Net	0.6783	0.3892	0.9845	0.9647

Fig. 8 shows an exemplar graphical comparison of temperature distribution predictions with an unforeseen test dataset. All three network models exhibit results closely resembling the target temperature distribution. Consistent with the results in Table 5, both U-Net and Attention U-Net demonstrate higher accuracy in all evaluation metrics compared to EDCNN. While the weighted Dice scores of U-Net and Attention U-Net are comparable, Attention U-Net shows a lower RMSE and MAE. This means that the temperature distribution greater than 50°C can be predicted with an accuracy of within 0.7% by the use of Attention U-Net.

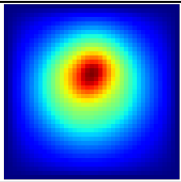
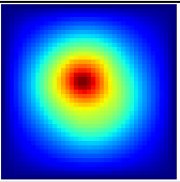
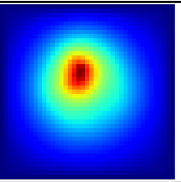
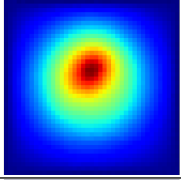
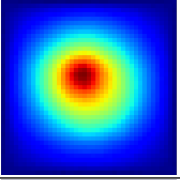
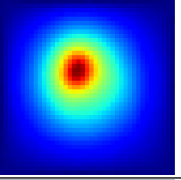
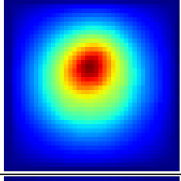
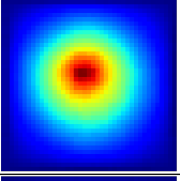
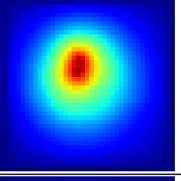
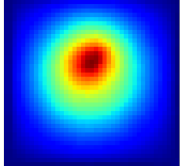
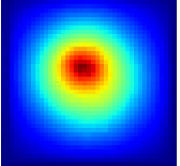
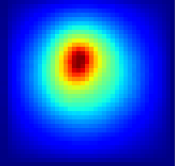
methods	xy	yz	zx	RMSE	MAE	Dice <sub>(&gt;40)</sub>	Dice <sub>(&gt;50)</sub>
Target							
EDCNN				0.6570	0.4628	0.9783	0.9537
U-Net				0.5082	0.3233	0.9909	0.9769
Att. U-Net				0.4746	0.2580	0.9936	0.9882

Figure 8: Comparison of temperature distribution predictions from various networks on an unforeseen test dataset with simulation results for a single sample.

Fig. 9 and Fig. 10 show the box plot of the ablation lesion volume and thermal distribution, respectively. In both cases, it is obvious that the order of prediction accuracy, from lowest to highest, is EDCNN, followed by U-Net, and then Attention U-Net.

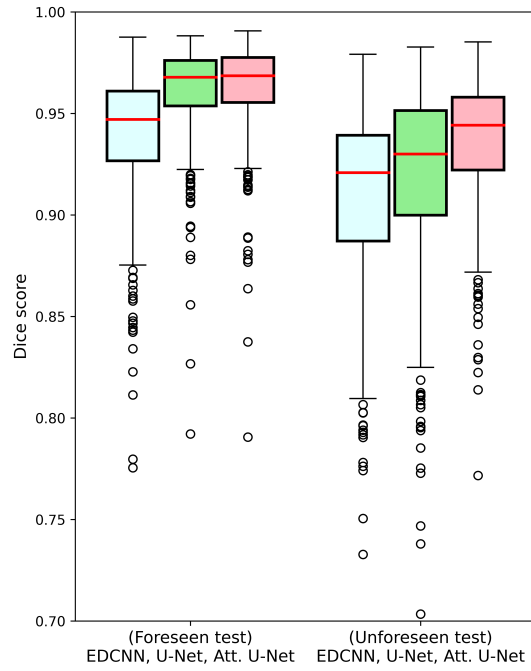


Figure 9: Dice score results for the ablation lesion zone with the methods of EDCNN, U-Net, and Attention U-Net. The three on the left were evaluated using a foreseen dataset, while the three on the right were assessed with an unforeseen dataset. The median value is denoted by the red horizontal line, while the interquartile range (IQR: from Q1 to Q3) is represented by the rectangle.

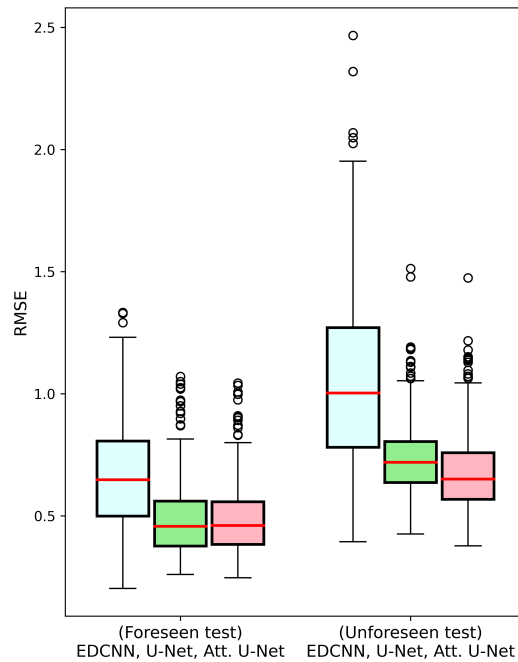


Figure 10: RMSE evaluations for the temperature distribution with the methods of EDCNN, U-Net, and Attention U-Net. The three on the left were evaluated using a foreseen dataset, while the three on the right were assessed with an unforeseen dataset. The median value is denoted by the red horizontal line, while the interquartile range (IQR: from Q1 to Q3) is represented by the rectangle.

## 4.5 Evaluation of inference time

In this section, we present a comparison of inference times across three different network architectures to assess their suitability for real-time inference. As shown in Table 6, the inference times for EDCNN, U-Net, and Attention U-Net are approximately 1.49, 2.16, and 8.51 ms, respectively. This implies that the prediction of thermal effects (i.e., ablation lesion zone and temperature distribution) during RFA treatment can be completed in just under 10 ms with two inputs; the segmented breast tumor MR image and placement of ablation tip setup. The inference time was measured using parallel GPU computation in a desktop computer of AMD Ryzen 9 5900x 12-core processor 3.70 GHz and NVIDIA GeForce RTX 3090.

Table 6: Comparisons of inference times across different network architectures.

networks	inference time (ms)
EDCNN	1.4854
U-Net	2.1557
Attention U-Net	8.5140

## 5 Concluding remarks

Digital twin, a representation of real-world objects, processes, and systems in a virtual space, stands at the forefront of the digital transformation era. In the healthcare domain, its application holds the potential to precisely monitor treatment processes and analyze patients' conditions, paving the way for personalized therapies and diagnostics. One crucial point in realizing this technology is the real-time simulation of physical phenomena occurring in the target object. Recent efforts have integrated mathematical analysis models with artificial intelligence (AI) techniques, resulting in the creation of AI models capable of real-time inference of physical phenomena. In this paper, we proposed physics-guided network models that can provide real-time feedback information on the thermal effects occurring during RFA treatment to users. The developed model achieved a 96% accuracy in predicting the ablation lesion volume in terms of the Dice score and showed a temperature distribution difference of 0.4854 in terms of RMSE evaluation. Even in the evaluation using unforeseen data, the network demonstrated robust performance with a 93% Dice score for ablation lesion prediction and a 0.6783 RMSE for temperature prediction. Furthermore, all network models exhibited real-time capabilities, inferring thermal effects within 10 ms (over 100 frames per second), using only standard home desktop computer specifications.

To assess the robustness of the networks for new patients, we conducted an accuracy evaluation using unforeseen data not involved in the training of the network model. As presented in Table 3 and 5, the results indicated a minor decline in performance compared to results from data previously seen during training. Nevertheless, the networks still achieved high accuracy levels, highlighting the generality of the PhysRFANet and its capacity to adapt accurately to new breast tumor MR image data from new patients.

While the use of *ex vivo* bovine liver tissue in the experiments provided validation of our models, it is crucial to acknowledge deficiency in replicating the dynamic physiological conditions inherent in living human patients [59]. The differences between bovine and human organs such as spatial relationships with other heat-sensitive organs, tissue cooling by the neighboring blood vessels [60], blood flow dynamics [61], immune response [62], and other metabolic activities, may impact the generalizability of our results to human clinical scenarios. Despite this limitation, the use of *ex vivo* bovine liver tissue offers a practical approach for preliminary investigations, laying the groundwork for further studies in more complex and clinically relevant settings.

This study did not account for RFA needle deflection or displacement [63, 64] or deformation of the patient's breast tissue [65] during RFA tip insertion. Neglecting these aspects could potentially impact the accuracy of the RFA procedure, as the tissue displacement resulting from changes in breast shape

and needle deflection during tip insertion must be considered for precise treatment planning. Addressing these factors represents a promising avenue for future research endeavors.

To effectively utilize the developed models in clinical practice, it needs to be integrated with a technique for precisely placing RFA electrodes. For example, fusion imaging technology, specifically the integration of CT/MR-US fusion imaging, has significantly improved the accuracy of guiding RFA treatment [66, 67, 68, 69]. The integrated approach of the PhysRFANet and fusion imaging technology can lead to a more targeted and effective application of RFA, thereby minimizing procedural errors and optimizing therapeutic outcomes.

In conclusion, this study introduces a novel approach that leverages physics-guided network models to provide real-time feedback on thermal effects during RFA treatment. Through MR images from 13 actual breast cancer patients, our approach has been verified to accurately infer patient-specific characteristics of the multi-biophysics phenomena occurring during RFA procedures. The proposed deep learning-based model holds great promise not only in advancing the standards of medical interventions and ensuring the safety and efficacy of RFA treatment but also in broadening the scope of RFA applications.

## Acknowledgments

The work was supported in part by the Korea Institute of Science and Technology (KIST) Institutional Program under Grant 2E31071, and in part by the National Research Foundation of Korea (NRF) grant funded by the Korean government (MSIT) (No. RS-2023-00220762).

## Data and software availability

The dataset, source code, and the description are available at <https://github.com/iangilan/PhysRFANet>.

## Declaration of competing interest

The authors declare no competing interests.

## References

- [1] S. McDermott, D. A. Gervais, Radiofrequency ablation of liver tumors, *Semin. Intervent. Radiol.* 30 (2013) 49–55. doi:[10.1055/s-0033-1333653](https://doi.org/10.1055/s-0033-1333653).
- [2] F. Zhu, H. Rhim, Thermal ablation for hepatocellular carcinoma: what’s new in 2019, *Chin. Clin. Oncol.* 8 (2019). doi:[10.21037/cco.2019.11.03](https://doi.org/10.21037/cco.2019.11.03).
- [3] A. M. Abd El-Kader, H. E. Ali, M. A. Gad, B. A. Abdel Aziz, S. E. A. Hassanien, A. Hasaneen, R. A. Mitwally, Percutaneous radiofrequency ablation compared with surgical resection in the treatment of early hepatocellular carcinoma, *Egypt. J. Surg.* 37 (2018). doi:[10.4103/ejs.ejs\\_97\\_17](https://doi.org/10.4103/ejs.ejs_97_17).
- [4] S. Yap, E. H. Ooi, J. J. Foo, E. T. Ooi, Comparisons between impedance-based and time-based switching bipolar radiofrequency ablation for the treatment of liver cancer, *Comput. Biol. Med.* 134 (2021) 104488. doi:[10.1016/j.combiomed.2021.104488](https://doi.org/10.1016/j.combiomed.2021.104488).
- [5] M. C. L. Peek, M. Douek, Ablative techniques for the treatment of benign and malignant breast tumours, *J. Ther. Ultrasound* 5 (2017) 18. doi:[10.1186/s40349-017-0097-8](https://doi.org/10.1186/s40349-017-0097-8).
- [6] H. K. Lim, Radiofrequency thermal ablation of hepatocellular carcinomas, *Korean J. Radiol.* 1 (2000) 175–184. doi:[10.3348/kjr.2000.1.4.175](https://doi.org/10.3348/kjr.2000.1.4.175).
- [7] Q. Zhu, Y. Shen, A. Zhang, L. X. Xu, Numerical study of the influence of water evaporation on radiofrequency ablation, *Biomed. Eng. Online* 12 (2013) 127. doi:[10.1186/1475-925X-12-127](https://doi.org/10.1186/1475-925X-12-127).



- [8] E. J. Berjano, Theoretical modeling for radiofrequency ablation: state-of-the-art and challenges for the future, *Biomed. Eng. Online* 5 (2006) 24. doi:[10.1186/1475-925X-5-24](https://doi.org/10.1186/1475-925X-5-24).
- [9] L. D. Ho, L. J. Min, Recent advances in the image-guided tumor ablation of liver malignancies: Radiofrequency ablation with multiple electrodes, real-time multimodality fusion imaging, and new energy sources, *Korean J. Radiol.* 19 (2018) 545–559. doi:[10.3348/kjr.2018.19.4.545](https://doi.org/10.3348/kjr.2018.19.4.545).
- [10] G. Widmann, G. Bodner, R. Bale, Tumour ablation: technical aspects, *Cancer Imaging* 9 Spec No A (2009) S63–7. doi:[10.1102/1470-7330.2009.9026](https://doi.org/10.1102/1470-7330.2009.9026).
- [11] S. Mulier, R. Possebon, Y. Jiang, J. Jamart, C. Wang, Y. Miao, T. Yu, K. Jiang, Y. Feng, G. Marchal, L. Michel, Y. Ni, Radiofrequency ablation with four electrodes as a building block for matrix radiofrequency ablation: Ex vivo liver experiments and finite element method modelling. influence of electric and activation mode on coagulation size and geometry, *Surg. Oncol.* 33 (2020) 145–157. doi:[10.1016/j.suronc.2020.02.005](https://doi.org/10.1016/j.suronc.2020.02.005).
- [12] Y. Jiang, S. Mulier, C. Wang, M. Cristiane, D. Rambo, F. Chen, G. Marchal, Y. Ni, S. Chong, G. Ni, Formulation of 3D finite elements for hepatic radiofrequency ablation, *Int. J. Model. Identif. Control.* 9 (2010) 225–235. doi:[10.1504/IJMIC.2010.032803](https://doi.org/10.1504/IJMIC.2010.032803).
- [13] E. S. McCreedy, R. Cheng, P. F. Hemler, A. Viswanathan, B. J. Wood, M. J. McAuliffe, Radio frequency ablation registration, segmentation, and fusion tool, *IEEE Trans. Inf. Technol. Biomed.* 10 (2006) 490–496. doi:[10.1109/titb.2006.872076](https://doi.org/10.1109/titb.2006.872076).
- [14] D. Bertaccini, D. Calvetti, Fast simulation of solid tumors thermal ablation treatments with a 3D reaction diffusion model, *Comput. Biol. Med.* 37 (2007) 1173–1182. doi:[10.1016/j.compbimed.2006.10.008](https://doi.org/10.1016/j.compbimed.2006.10.008).
- [15] R. Barauskas, A. Gulbinas, T. Vanagas, G. Barauskas, Finite element modeling of cooled-tip probe radiofrequency ablation processes in liver tissue, *Comput. Biol. Med.* 38 (2008) 694–708. doi:[10.1016/j.compbimed.2008.03.007](https://doi.org/10.1016/j.compbimed.2008.03.007).
- [16] Y. Shao, B. Arjun, H. Leo, K. Chua, A computational theoretical model for radiofrequency ablation of tumor with complex vascularization, *Comput. Biol. Med.* 89 (2017) 282–292. doi:[10.1016/j.compbimed.2017.08.025](https://doi.org/10.1016/j.compbimed.2017.08.025).
- [17] E. H. Ooi, K. W. Lee, S. Yap, M. A. Khattab, I. Y. Liao, E. T. Ooi, J. J. Foo, S. R. Nair, A. F. Mohd Ali, The effects of electrical and thermal boundary condition on the simulation of radiofrequency ablation of liver cancer for tumours located near to the liver boundary, *Comput. Biol. Med.* 106 (2019) 12–23. doi:[10.1016/j.compbimed.2019.01.003](https://doi.org/10.1016/j.compbimed.2019.01.003).
- [18] T. Kröger, I. Altrogge, T. Preusser, P. Pereira, D. Schmidt, A. Weihusen, H.-O. Peitgen, Numerical simulation of radio frequency ablation with state dependent material parameters in three space dimensions, in: *Medical Image Computing and Computer-Assisted Intervention – MICCAI 2006*. MICCAI 2006. Lecture Notes in Computer Science, vol 4191, volume 9, 2006, pp. 380–8. doi:[10.1007/11866763\\_47](https://doi.org/10.1007/11866763_47).
- [19] A. V. Shahidi, P. Savard, A finite element model for radiofrequency ablation of the myocardium, *IEEE. Trans. Biomed. Eng.* 41 (1994) 963–968. doi:[10.1109/10.324528](https://doi.org/10.1109/10.324528).
- [20] S. Singh, R. Repaka, Quantification of thermal injury to the healthy tissue due to imperfect electrode placements during radiofrequency ablation of breast tumor, *J. Eng. Sci. Med. Diagn. Ther.* 1 (2018) 011002. doi:[10.1115/1.4038237](https://doi.org/10.1115/1.4038237).
- [21] P. Voglreiter, P. Mariappan, M. Pollari, R. Flanagan, R. Blanco Sequeiros, R. H. Portugaller, J. Fütterer, D. Schmalstieg, M. Kolesnik, M. Moche, RFA Guardian: Comprehensive simulation of radiofrequency ablation treatment of liver tumors, *Sci. Rep.* 8 (2018) 787. doi:[10.1038/s41598-017-18899-2](https://doi.org/10.1038/s41598-017-18899-2).

- [22] P. Mariappan, P. Weir, R. Flanagan, P. Voglreiter, T. Alhonnoro, M. Pollari, M. Moche, H. Busse, J. Futterer, H. R. Portugaller, R. B. Sequeiros, M. Kolesnik, GPU-based RFA simulation for minimally invasive cancer treatment of liver tumours, *Int. J. Comput. Assist. Radiol. Surg.* 12 (2017) 59–68. doi:[10.1007/s11548-016-1469-1](https://doi.org/10.1007/s11548-016-1469-1).
- [23] N. Kath, H. Handels, A. Mastmeyer, Robust GPU-based virtual reality simulation of radio-frequency ablations for various needle geometries and locations, *Int. J. Comput. Assist. Radiol. Surg.* 14 (2019) 1825–1835. doi:[10.1007/s11548-019-02033-w](https://doi.org/10.1007/s11548-019-02033-w).
- [24] E. K. Hoffer, A. Borsic, S. D. Patel, Validation of software for patient-specific real-time simulation of hepatic radiofrequency ablation, *Acad. Radiol.* 29 (2022) e219–e227. doi:[10.1016/j.acra.2021.12.018](https://doi.org/10.1016/j.acra.2021.12.018).
- [25] A. Akbari, D. Giannacopoulos, An efficient multi-threaded Newton–Raphson algorithm for strong coupling modeling of multi-physics problems, *Comput. Phys. Commun.* 258 (2021) 107563. doi:[10.1016/j.cpc.2020.107563](https://doi.org/10.1016/j.cpc.2020.107563).
- [26] J. Abraham, E. Sparrow, A thermal-ablation bioheat model including liquid-to-vapor phase change, pressure- and necrosis-dependent perfusion, and moisture-dependent properties, *Int. J. Heat Mass Transf.* 50 (2007) 2537–2544. doi:<https://doi.org/10.1016/j.ijheatmasstransfer.2006.11.045>.
- [27] M. Lutter, C. Ritter, J. Peters, Deep Lagrangian Networks: Using physics as model prior for deep learning, arXiv preprint arXiv:1907.04490 (2019). doi:[10.48550/arXiv.1907.04490](https://doi.org/10.48550/arXiv.1907.04490).
- [28] A. Mendizabal, P. Márquez-Neila, S. Cotin, Simulation of hyperelastic materials in real-time using deep learning, *Med. Image Anal.* 59 (2020) 101569. doi:[10.1016/j.media.2019.101569](https://doi.org/10.1016/j.media.2019.101569).
- [29] M. Choi, M. Jang, S.-S. Yoo, G. Noh, K. Yoon, Deep neural network for navigation of a single-element transducer during transcranial focused ultrasound therapy: Proof of concept, *IEEE J. Biomed. Health Inform.* 26 (2022) 5653–5664. doi:[10.1109/JBHI.2022.3198650](https://doi.org/10.1109/JBHI.2022.3198650).
- [30] Y. Salehi, D. Giannacopoulos, PhysGNN: A physics-driven graph neural network based model for predicting soft tissue deformation in image-guided neurosurgery, *Adv. Neural Inf. Process. Syst.* 35 (2022) 37282–37296. doi:[10.48550/arXiv.2109.04352](https://doi.org/10.48550/arXiv.2109.04352).
- [31] M. Shin, Z. Peng, H.-J. Kim, S.-S. Yoo, K. Yoon, Multivariable-incorporating super-resolution residual network for transcranial focused ultrasound simulation, *Comput. Methods Programs Biomed.* 237 (2023) 107591. doi:[10.1016/j.cmpb.2023.107591](https://doi.org/10.1016/j.cmpb.2023.107591).
- [32] E. Besler, Y. C. Wang, A. V. Sahakian, Real-time radiofrequency ablation lesion depth estimation using multi-frequency impedance with a deep neural network and tree-based ensembles, *IEEE Trans. Biomed. Eng.* 67 (2020) 1890–1899. doi:[10.1109/TBME.2019.2950342](https://doi.org/10.1109/TBME.2019.2950342).
- [33] A. Saha, M. R. Harowicz, L. J. Grimm, C. E. Kim, S. V. Ghate, R. Walsh, M. A. Mazurowski, A machine learning approach to radiogenomics of breast cancer: a study of 922 subjects and 529 DCE-MRI features, *Br. J. Cancer.* 119 (2018) 508–516. doi:[10.1038/s41416-018-0185-8](https://doi.org/10.1038/s41416-018-0185-8).
- [34] W. Burger, M. J. Burge, Principles of digital image processing, volume 111, Springer, 2009.
- [35] S. Singh, R. Repaka, Temperature-controlled radiofrequency ablation of different tissues using two-compartment models, *Int. J. Hyperth.* 33 (2017) 122–134. doi:[10.1080/02656736.2016.1223890](https://doi.org/10.1080/02656736.2016.1223890).
- [36] C. Schumann, T. Kroeger, C. Rieder, H. K. Hahn, GPU-based real-time approximation of the ablation zone for radiofrequency ablation, *IEEE Trans. Vis. Comput. Graph.* 17 (2011) 1812–1821. doi:[10.1109/TVCG.2011.207](https://doi.org/10.1109/TVCG.2011.207).

- [37] Z. Zhao, J. Song, X. Zhu, J. Wang, J. Wu, Y. Liu, Z.-P. Nie, Q. H. Liu, System development of microwave induced thermo-acoustic tomography and experiments on breast tumor, *Prog. Electromagn. Res.* 134 (2013) 323–336. doi:[10.2528/Pier12101604](https://doi.org/10.2528/Pier12101604).
- [38] H. H. Pennes, Analysis of tissue and arterial blood temperatures in the resting human forearm, *J. Appl. Physiol.* 1 (1948) 93–122. doi:[10.1152/jappl.1948.1.2.93](https://doi.org/10.1152/jappl.1948.1.2.93).
- [39] S. Labonte, Numerical model for radio-frequency ablation of the endocardium and its experimental validation, *IEEE. Trans. Biomed. Eng.* 41 (1994) 108–115. doi:[10.1109/10.284921](https://doi.org/10.1109/10.284921).
- [40] H.-J. Kim, S.-H. Um, Y. G. Kang, M. Shin, H. Jeon, B.-M. Kim, D. Lee, K. Yoon, Laser–tissue interaction simulation considering skin-specific data to predict photothermal damage lesions during laser irradiation, *J. Comput. Des. Eng.* 10 (2023) 947–958. doi:[10.1093/jcde/qwad033](https://doi.org/10.1093/jcde/qwad033).
- [41] F. C. Henriques Jr, Studies of thermal injury; the predictability and the significance of thermally induced rate processes leading to irreversible epidermal injury, *Arch. Pathol.* 43 (1947) 489–502.
- [42] J. Ma, Y. He, F. Li, L. Han, C. You, B. Wang, Segment anything in medical images, 2023. doi:[10.48550/arXiv.2304.12306](https://doi.org/10.48550/arXiv.2304.12306).
- [43] J. Ma, Y. He, F. Li, L. Han, C. You, B. Wang, Segment Anything in Medical Images, <https://github.com/bowang-lab/MedSAM>, 2023. Accessed: 2023-10-27.
- [44] D. Fuentes, R. Cardan, R. J. Stafford, J. Yung, G. D. Dodd III, Y. Feng, High-fidelity computer models for prospective treatment planning of radiofrequency ablation with in vitro experimental correlation, *J. Vasc. Interv. Radiol.* 21 (2010) 1725–1732. doi:[10.1016/j.jvir.2010.07.022](https://doi.org/10.1016/j.jvir.2010.07.022).
- [45] N. P. Silva, A. Bottiglieri, R. C. Conceição, M. O’Halloran, L. Farina, Characterisation of ex vivo liver thermal properties for electromagnetic-based hyperthermic therapies, *Sensors* 20 (2020) 3004. doi:<https://doi.org/10.3390/s20103004>.
- [46] M. Drozdal, E. Vorontsov, G. Chartrand, S. Kadoury, C. Pal, The importance of skip connections in biomedical image segmentation, in: G. Carneiro, D. Mateus, L. Peter, A. Bradley, J. M. R. S. Tavares, V. Belagiannis, J. P. Papa, J. C. Nascimento, M. Loog, Z. Lu, J. S. Cardoso, J. Cornebise (Eds.), *Deep Learning and Data Labeling for Medical Applications*, Springer International Publishing, Cham, 2016, pp. 179–187. doi:[10.1007/978-3-319-46976-8\\_19](https://doi.org/10.1007/978-3-319-46976-8_19).
- [47] K. He, X. Zhang, S. Ren, J. Sun, Deep residual learning for image recognition, in: *2016 IEEE Conference on Computer Vision and Pattern Recognition (CVPR)*, 2016, pp. 770–778. doi:[10.1109/CVPR.2016.90](https://doi.org/10.1109/CVPR.2016.90).
- [48] G. Huang, Z. Liu, L. Van Der Maaten, K. Q. Weinberger, Densely connected convolutional networks, in: *2017 IEEE Conference on Computer Vision and Pattern Recognition (CVPR)*, 2017, pp. 2261–2269. doi:[10.1109/CVPR.2017.243](https://doi.org/10.1109/CVPR.2017.243).
- [49] B. Hariharan, P. Arbeláez, R. Girshick, J. Malik, Hypercolumns for object segmentation and fine-grained localization, in: *2015 IEEE Conference on Computer Vision and Pattern Recognition (CVPR)*, 2015, pp. 447–456. doi:[10.1109/CVPR.2015.7298642](https://doi.org/10.1109/CVPR.2015.7298642).
- [50] T.-Y. Lin, P. Dollár, R. Girshick, K. He, B. Hariharan, S. Belongie, Feature pyramid networks for object detection, in: *2017 IEEE Conference on Computer Vision and Pattern Recognition (CVPR)*, 2017, pp. 936–944. doi:[10.1109/CVPR.2017.106](https://doi.org/10.1109/CVPR.2017.106).
- [51] Z. Zhou, M. M. Rahman Siddiquee, N. Tajbakhsh, J. Liang, UNet++: A nested U-Net architecture for medical image segmentation, in: D. Stoyanov, Z. Taylor, G. Carneiro, T. Syeda-Mahmood, A. Martel, L. Maier-Hein, J. M. R. Tavares, A. Bradley, J. P. Papa, V. Belagiannis, J. C. Nascimento, Z. Lu, S. Conjeti, M. Moradi, H. Greenspan, A. Madabhushi (Eds.), *Deep Learning in Medical Image*

Analysis and Multimodal Learning for Clinical Decision Support, Springer International Publishing, Cham, 2018, pp. 3–11. doi:[10.1007/978-3-030-00889-5\\_1](https://doi.org/10.1007/978-3-030-00889-5_1).

- [52] Y. Zhang, X. Zhan, J. Xiong, S. Peng, W. Huang, R. Joshi, Y. Cai, Y. Liu, R. Li, K. Yuan, N. Zhou, W. Min, Temperature-dependent cell death patterns induced by functionalized gold nanoparticle photothermal therapy in melanoma cells, *Sci. Rep.* 8 (2018) 8720. doi:[10.1038/s41598-018-26978-1](https://doi.org/10.1038/s41598-018-26978-1).
- [53] T. Sorenson, A method of establishing groups of equal amplitude in plant sociology based on similarity of species and its application to analyses of the vegetation on danish commons, *K. dansk. Vidensk. Selsk. Skr.* 5 (1948) 1–34.
- [54] L. R. Dice, Measures of the amount of ecologic association between species, *Ecology* 26 (1945) 297–302. doi:[10.2307/1932409](https://doi.org/10.2307/1932409).
- [55] P. Jaccard, The distribution of the flora in the Alpine zone.1, *New Phytol.* 11 (1912) 37–50. doi:[10.1111/j.1469-8137.1912.tb05611.x](https://doi.org/10.1111/j.1469-8137.1912.tb05611.x).
- [56] R. T. Rockafellar, R. J. B. Wets, *Variational analysis*, volume 317, Springer, 1998.
- [57] SciPy, SciPy User Guide, [https://docs.scipy.org/doc/scipy/reference/generated/scipy.ndimage.center\\_of\\_mass.html](https://docs.scipy.org/doc/scipy/reference/generated/scipy.ndimage.center_of_mass.html), 2023. Accessed: 2023-11-15.
- [58] C. A. Schneider, W. S. Rasband, K. W. Eliceiri, NIH image to ImageJ: 25 years of image analysis, *Nat. Methods* 9 (2012) 671–675. doi:[10.1038/nmeth.2089](https://doi.org/10.1038/nmeth.2089).
- [59] Y. N. Kim, H. Rhim, D. Choi, Y. sun Kim, M. W. Lee, I. Chang, W. J. Lee, H. K. Lim, The effect of radiofrequency ablation on different organs: Ex vivo and in vivo comparative studies, *Eur. J. Radiol.* 80 (2011) 526–532. doi:[10.1016/j.ejrad.2009.11.011](https://doi.org/10.1016/j.ejrad.2009.11.011).
- [60] B. M. Künzli, P. Abitabile, C. A. Maurer, Radiofrequency ablation of liver tumors: Actual limitations and potential solutions in the future, *World J. Hepatol.* 3 (2011) 8–14. doi:[10.4254/wjh.v3.i1.8](https://doi.org/10.4254/wjh.v3.i1.8).
- [61] E. J. Patterson, C. H. Scudamore, D. A. Owen, A. G. Nagy, A. K. Buczkowski, Radiofrequency ablation of porcine liver in vivo: Effects of blood flow and treatment time on lesion size, *Ann. Surg.* 227 (1998). doi:[10.1097/0000658-199804000-00018](https://doi.org/10.1097/0000658-199804000-00018).
- [62] M. Mauda-Havakuk, N. M. Hawken, J. W. Owen, A. S. Mikhail, A. Saxena, B. Karim, P. G. Wakim, W. F. Pritchard, J. W. Karanian, B. J. Wood, Comparative analysis of the immune response to RFA and cryoablation in a colon cancer mouse model, *Sci. Rep.* 12 (2022) 18229. doi:[10.1038/s41598-022-22279-w](https://doi.org/10.1038/s41598-022-22279-w).
- [63] T. L. de Jong, C. Klink, A. Moelker, J. Dankelman, J. J. van den Dobbelsteen, Needle deflection in thermal ablation procedures of liver tumors: a CT image analysis, in: B. Fei, R. J. Webster (Eds.), *Medical Imaging 2018: Image-Guided Procedures, Robotic Interventions, and Modeling*, volume 10576 of *Society of Photo-Optical Instrumentation Engineers (SPIE) Conference Series*, 2018, p. 105761L. doi:[10.1117/12.2292884](https://doi.org/10.1117/12.2292884).
- [64] J. J. Pérez, E. Nadal, E. Berjano, A. González-Suárez, Computer modeling of radiofrequency cardiac ablation including heartbeat-induced electrode displacement, *Comput. Biol. Med.* 144 (2022) 105346. doi:[10.1016/j.combiomed.2022.105346](https://doi.org/10.1016/j.combiomed.2022.105346).
- [65] M. Danch-Wierzchowska, D. Borys, A. Swierniak, FEM-based MRI deformation algorithm for breast deformation analysis, *Biocybern. Biomed. Eng.* 40 (2020) 1304–1313. doi:[10.1016/j.bbe.2020.07.009](https://doi.org/10.1016/j.bbe.2020.07.009).

- [66] J. P. McWilliams, E. W. Lee, S. Yamamoto, C. T. Loh, S. T. Kee, Image-guided tumor ablation: emerging technologies and future directions, *Semin. Intervent. Radiol.* 27 (2010) 302–313. doi:[10.1055/s-0030-1261789](https://doi.org/10.1055/s-0030-1261789).
- [67] Y. Makino, Y. Imai, T. Igura, S. Kogita, Y. Sawai, K. Fukuda, T. Iwamoto, J. Okabe, M. Takamura, N. Fujita, M. Hori, T. Takehara, M. Kudo, T. Murakami, Feasibility of extracted-overlay fusion imaging for intraoperative treatment evaluation of radiofrequency ablation for hepatocellular carcinoma, *Liver Cancer* 5 (2016) 269–279. doi:[10.1159/000449338](https://doi.org/10.1159/000449338).
- [68] B. J. Wood, J. Kruecker, N. Abi-Jaoudeh, J. K. Locklin, E. Levy, S. Xu, L. Solbiati, A. Kapoor, H. Amalou, A. M. Venkatesan, Navigation systems for ablation, *J. Vasc. Interv. Radiol.* 21 (2010) S257–S263. *Thermal Ablation 2010: At the Crossroads of Past Success, Current Goals, and Future Technology*. doi:[10.1016/j.jvir.2010.05.003](https://doi.org/10.1016/j.jvir.2010.05.003).
- [69] J. Kruecker, S. Xu, A. Venkatesan, J. K. Locklin, H. Amalou, N. Glossop, B. J. Wood, Clinical utility of real-time fusion guidance for biopsy and ablation, *J. Vasc. Interv. Radiol.* 22 (2011) 515–524. doi:[10.1016/j.jvir.2010.10.033](https://doi.org/10.1016/j.jvir.2010.10.033).